Journal of *Marine Science and Engineering*

MDPI

Article

Observed Wave Characteristics and Tropical-Cyclone-Induced Spectral Evolution East of Hainan Island

Yunlong Ma, Xiaohua Zhu *, Dingyong Zeng, Feilong Lin and Xiaobo Ni

State Key Laboratory of Satellite Ocean Environment Dynamics, Second Institute of Oceanography, Ministry of Natural Resources, Hangzhou 310012, China; ylma@sio.org.cn (Y.M.)
* Correspondence: xhzhu@sio.org.cn

Abstract

A comprehensive understanding of the regional wave conditions has become increasingly important for structural design, operational safety, and marine hazard prevention. Continuous directional wave measurements in the deeper offshore waters east of Hainan Island remain limited. This study examined the wave characteristics and tropical cyclone-induced spectral evolution east of Hainan Island using nine months of directional wave observations collected at a water depth of approximately 120 m. The monthly mean significant wave height $H_{1/3}$ ranged from 0.80 to 2.81 m, with a maximum observed $H_{1/3}$ of 4.56 m, while the monthly mean significant wave period $T_{1/3}$ ranged from 5.01 to 8.61 s; waves from the ENE and E waves were dominant. The baseline ERA5-based classification indicated a predominance of swell-dominated mixed seas (58%), although ±1 RMSE wind-speed perturbations substantially altered the class proportions. In contrast, pure wind seas consistently showed the strongest wind–wave directional agreement across all sensitivity scenarios, with 68.4–75.5% of cases within 22.5° and 95.2–97.1% within 45°. Among the two tropical cyclones affecting the study region, Tropical Storm Maliksi produced a stronger local wave response than that of Severe Tropical Storm Prapiroon, with mean $H_{1/3}$ values of 2.06 and 1.49 m, respectively. During Maliksi, the spectral density increased markedly near 0.10–0.12 Hz, while the pre-storm double-peaked spectrum evolved into a stronger, directionally concentrated dominant component. These findings provide site-specific observational evidence of wave variability and tropical cyclone-induced spectral evolution east of Hainan Island, offering a reference for regional wave characterization and wave-model evaluation.

Keywords: South China Sea; offshore waters east of Hainan Island; wave characteristics; tropical cyclone waves; wave spectrum; in situ observation

Check for updates

Academic Editor: Eugen Rusu

Received: 7 October 2026
Revised: 25 October 2026
Accepted: 26 October 2026
Published: 29 October 2026

Copyright: © 2026 by the authors. Licensee MDPI, Basel, Switzerland. This article is an open access article distributed under the terms and conditions of the Creative Commons Attribution (CC BY) license.

1. Introduction

The South China Sea (SCS) is characterized by pronounced seasonal and event-scale variabilities in wind and wave conditions. The regional wave climate is strongly influenced by monsoonal forcing and tropical cyclones, resulting in substantial variations in wave height, period, and direction over different temporal scales [1,2]. With the continued development of offshore wind farms, oil and gas platforms, marine transportation, and other offshore engineering activities in the northern SCS, a comprehensive understanding of the regional wave conditions has become increasingly important for structural design, operational safety, and marine hazard prevention. In particular, tropical cyclone-generated waves can induce considerable loads on offshore structures, and their accurate characterization continues to be a substantial challenge in engineering applications and wave prediction [3,4].

Wave characteristics have been investigated using numerical simulations, reanalysis products, satellite observations, and in situ measurements. Long-term numerical and reanalysis datasets are effective for characterizing the large-scale spatial and temporal variabilities of wind and wave conditions. For example, Dong et al. [5] examined the long-term wind and wave variations in the Taiwan Strait, whereas Hisaki [6] investigated the variability in wave height in the Sea of Japan. Jiang et al. [2] analyzed the evolution of wave energy resources along the Guangdong coast using long-term reanalysis data. However, direct field measurements remain particularly valuable for characterizing local wave conditions and evaluating the statistical relationships among the wave parameters. Therefore, buoy and field observations have been extensively used in coastal and offshore environments, including the Nowshahr Port [7], central Taiwan Strait [8], Pearl River Estuary [9], Haikou Bay [10], and Sanmen Bay [11,12]. Chen et al. [13] further demonstrated the effectiveness of in situ observations for regional wave assessment in the northern SCS, whereas Cai et al. [14] revealed distinct temporal variability in the observed wave conditions within the South China Sea lagoon. These studies highlighted the importance of field observations for regional wave assessment; however continuous directional wave measurements in the deeper offshore waters east of Hainan Island remain limited.

Tropical cyclones can rapidly modify the background wave field through strong and continuously varying wind forces. Tropical cyclone passage is typically accompanied by rapid increases in wave height, changes in characteristic wave periods, and substantial variations in wave direction and spectral structures. Yang et al. [15] investigated wave characteristics during several typhoons using observations from coastal waters northeast of Zhoushan Island, whereas Kumar et al. [16] examined the statistical characteristics of wave crest heights under tropical cyclone conditions. In the northern SCS, Yang et al. [17] analyzed the observed typhoon wave spectra and demonstrated distinct spectral characteristics under strong storm forcing. Cai et al. [18] further showed, using direct observations that typhoon-generated waves in the South China Sea reef lagoon exhibited notable changes in wave height and spectral properties during storm passage. Numerical studies have also demonstrated that a simulated typhoon wave response can be highly sensitive to the representation of a forcing wind field [3,4]. Therefore, bulk wave parameters capture only part of the storm response. Spectral analysis is also required to resolve changes in the wave energy distribution and relative contribution of different wave components during tropical cyclone passages.

Recent advances have broadened both the observational and modeling approaches used to investigate tropical-cyclone-related ocean and wave responses. High-resolution atmosphere–ocean–wave coupled modeling has increasingly been combined with data-driven forecasting systems; for example, Lai et al. [19] demonstrated that AI-model-driven regional coupled simulations can improve the representation and prediction of tropical-cyclone track, intensity, and fine-scale storm structure. Coastal wave responses can also be strongly modified by local environmental processes. Qiu et al. [20] showed that storm-induced wave attenuation by mangroves is controlled by coupled effects of storm waves and surge, highlighting the complexity of wave transformation in coastal environments. More recently, Lui et al. [21] combined aircraft, dropsonde, radar, wind-profiler, satellite, and surface observations with numerical forecasting to characterize Super Typhoon Fung-Wong over the South China Sea, further demonstrating the value of integrated observations for tropical-cyclone analysis and forecast evaluation.

Satellite observations provide an important complementary perspective on ocean wave fields. In particular, the Surface Waves Investigation and Monitoring (SWIM) instrument onboard CFOSAT provides broad-scale observations of wave parameters and directional wave spectra. Liang et al. [22] evaluated SWIM L2 products against buoy and altimeter

observations, while Tang et al. [23] assessed SWIM wave parameters and spectral products in the South China Sea and demonstrated their applicability to the characterization of wind-sea and swell components. Xu et al. [24] further compared directional wave spectra derived from SWIM with buoy observations at the spectral level. Satellite and buoy measurements nevertheless differ substantially in their sampling characteristics: satellite observations provide broad but intermittent spatial coverage, whereas moored directional buoys provide continuous local observations and can resolve short-term changes in wave height, period, direction, and spectral structure.

The interpretation of buoy measurements also depends strongly on the observational environment. Rybalko et al. [25], using a Datawell directional buoy at short-fetch nearshore sites in the Black Sea, showed that mixed sea states can dominate under shallow coastal conditions, where limited fetch, coastal geometry, and rapidly varying local winds strongly affect the wind-wave and swell components. The present observation site, located in approximately 120 m water depth in the deeper offshore waters east of Hainan Island, represents a distinctly different wave environment in which remotely generated swell can make a substantial contribution to the local sea state. These contrasts emphasize the need for long-duration in situ directional measurements to complement satellite and model products and to distinguish regional offshore wave characteristics from those observed in short-fetch coastal environments.

In this study, nine months of directional wave observations collected by a moored Waverider buoy at a water depth of approximately 120 m east of Hainan Island were analyzed. The monthly and overall wave height, period, and direction characteristics were first examined to describe the regional wave environment. The statistical relationships between the characteristic wave-height and wave period parameters were then evaluated and compared with those reported for other coastal and offshore regions. During the observation period, two tropical cyclones, the Tropical Storm Maliksi and Severe Tropical Storm Prapiroon, affected the northern South China Sea with distinct tracks and intensity evolutions (Figure 1). The two events were compared based on their bulk wave characteristics; subsequently, Maliksi was comprehensively examined using time series and spectral analyses. The baseline ERA5-based classification indicated a substantial contribution from swell-dominated mixed seas, while an RMSE-based wind-speed sensitivity test was conducted to assess how the estimated sea-state proportions respond to perturbations in ERA5 wind speed. Maliksi produced a stronger local wave response than Prapiroon, accompanied by pronounced spectral enhancement and increased directional concentration of the dominant spectral component. The observations characterize both background and cyclone-modified wave conditions east of Hainan Island and provide field-based reference information for offshore engineering and wave model evaluations in the northern South China Sea.

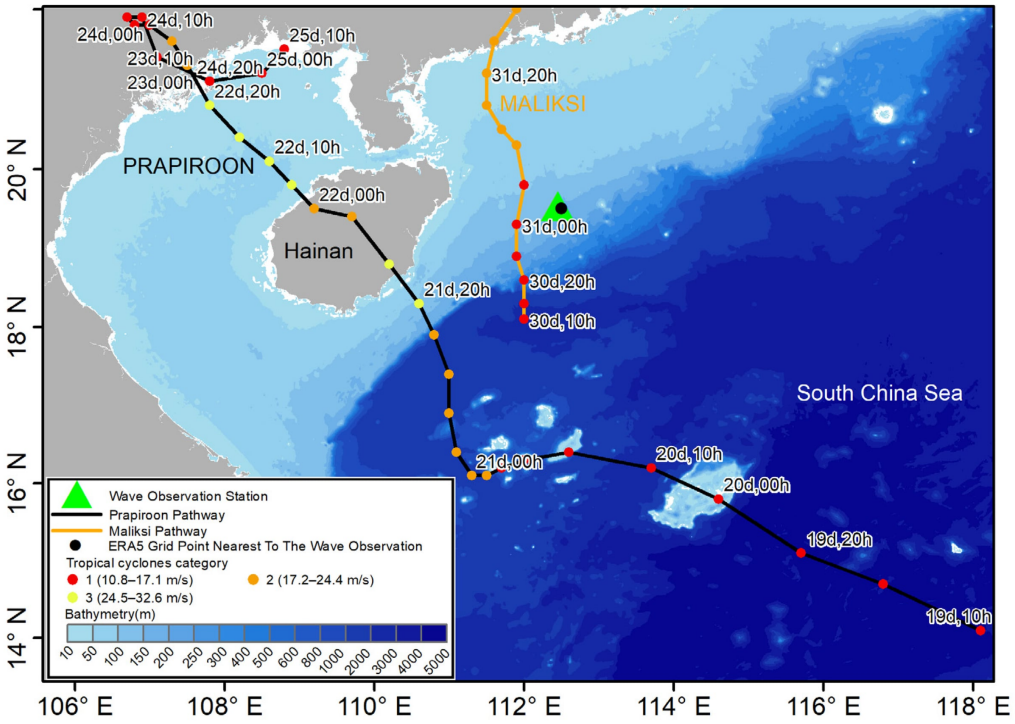


Figure 1. Study area and tracks of Tropical Storm Maliksi and Severe Tropical Storm Prapiroon during the observation period. The orange and black lines represent the tracks of Maliksi and Prapiroon, respectively, while the colored markers indicate cyclone intensity based on maximum sustained wind speed. The green triangle denotes the wave observation station, and the nearest ERA5 grid point is also indicated. The nearest ERA5 grid point is approximately 6.6 km from the buoy, with a model water depth of approximately 161 m.

2. Materials and Methods

2.1. Study Area and Observation Period

The observation site was located east of Hainan Island in the northern South China Sea at a water depth of approximately 120 m (Figure 1). The site was located approximately 500 m from the nearest offshore oil platform, making the observed wave conditions relevant to offshore engineering operations. Continuous wave observations were conducted from 1 December 2023 to 31 August 2024. During this period, the Tropical Storm Maliksi and Severe Tropical Storm Prapiroon affected the study region. Figure 1 shows the tracks of Tropical Storm Maliksi and Severe Tropical Storm Prapiroon, distinguished by orange and black lines, respectively, together with their intensity evolution and positions relative to the wave observation station. Tropical cyclone best-track data were obtained from the CMA-STI dataset [26,27].

2.2. Wave Observation System

Wave observations were obtained using a Datawell Directional Waverider MkIII buoy (Datawell BV, Haarlem, The Netherlands) deployed at the observation site (Figure 2). The mooring system consisted of a surface buoy, an elastic mooring line, and a seabed anchor, enabling the buoy to follow sea-surface motion while remaining within the vicinity of the deployment location.

The Datawell Directional Waverider MkIII measures sea-surface motion using onboard accelerometers. According to the manufacturer's specifications, the heave measurement range is −20 to +20 m, with a resolution of 0.01 m and an accuracy better than 0.5% of the measured value after calibration and better than 1.0% after three years of operation. The

measurable wave-period range is 1.6–30 s. Sea-surface motion was internally sampled at 3.84 Hz, digitally filtered, and downsampled to 1.28 Hz. The resulting 1.28 Hz displacement records were used for the wave-parameter and spectral analyses described below [28].

Data stored directly on the buoy memory card were used in this study to avoid data loss associated with wireless transmission. The stored surface-displacement records formed the basis of both the zero-upcrossing analysis and the frequency-domain spectral analysis.

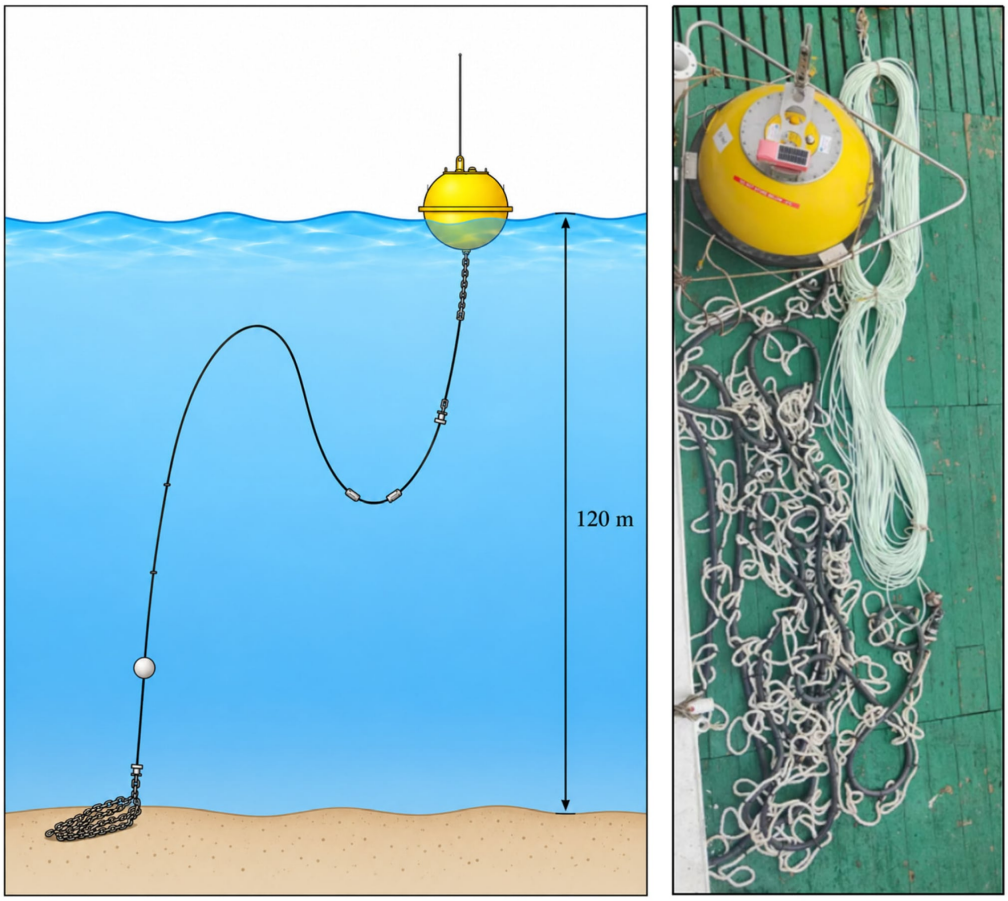


Figure 2. Configuration of the Datawell Directional Waverider MkIII buoy and mooring system used in this study: schematic of the deployment and mooring configuration at the approximately 120 m-deep observation site and photograph of the buoy and mooring components before deployment. The schematic was redrawn by the authors with reference to the general mooring configuration described in the official Datawell Waverider Reference Manual [28], and the photograph was taken during the field campaign.

2.3. Data Processing and Wave Spectrum Analysis

2.3.1. ERA5 Wind Data and Wind–Wave Directional Difference

Wind conditions during the observation period were characterized using ERA5 reanalysis data produced by the European Centre for Medium-Range Weather Forecasts (ECMWF). Hourly 10 m zonal and meridional wind components were extracted from the ERA5 grid point nearest to the wave observation site for the corresponding observation period. The 10 m wind speed, U_{10}, was calculated using the zonal and meridional wind components. The ERA5 wind direction was derived from these components using the meteorological conventions, with the directions indicating the origin of wind. The nearest ERA5 grid point was approximately 6.6 km from the buoy, with a model water depth of approximately 161 m, compared with the observational water depth of approximately 120 m.

ERA5 wave parameters were also extracted for comparison with the buoy observations. Significant wave height (SWH) and mean wave period (MWP) were obtained at the grid point corresponding to the observation site. For the full-period comparison, the 30 min buoy observations were linearly interpolated to the hourly ERA5 timestamps. ERA5 SWH was compared with buoy ($H_{1/3}$), whereas ERA5 MWP was compared with buoy ($T_{1/3}$) to assess the consistency of their temporal variability. The latter comparison was not treated as a strict parameter-equivalent validation because the two period measures are defined differently. Agreement was quantified using the correlation coefficient ((R)), bias, RMSE, and MAE, with bias defined as ERA5 minus buoy.

For the sea-state classification, hourly ERA5 wind speeds were linearly interpolated to the 30 min wave-observation timestamps. For the wind–wave directional-difference analysis, wave observations were matched to the corresponding hourly ERA5 records. Both the ERA5 wind direction and observed wave direction were expressed using the FROM convention. The signed directional difference between the wind and wave directions is calculated as follows:

$$\Delta\theta = \mathrm{mod}(\theta_{wave} - \theta_{wind} + 180°, 360°) - 180°, \quad (1)$$

where θ_{wave} and θ_{wind} denote the observed wave direction and ERA5 wind direction, respectively. The absolute directional difference, $|\Delta\theta|$, was used to quantify wind–wave directional agreement. A directional difference of 45° was used as a descriptive threshold to compare the directional agreement among the different sea-state classes.

These wind data were also compared with the observed variations in wave height, wave period, and wave direction to characterize the response of the local wave field to wind forcing and tropical cyclone passages.

2.3.2. ASCAT–ERA5 Wind Validation and Sea-State Sensitivity Analysis

Because no collocated in situ wind measurements were available at the buoy site, the ERA5 10 m winds used in the sea-state classification were independently evaluated against MetOp-B and MetOp-C ASCAT Level-2 coastal wind observations. For each ASCAT overpass, the nearest quality-controlled ASCAT wind vector cell (WVC) within 25 km of the buoy was retained. ERA5 zonal and meridional 10 m wind components were bilinearly interpolated to the geographic location of the selected ASCAT WVC and subsequently linearly interpolated in time to the exact ASCAT observation time. Wind speed was then reconstructed from the interpolated vector components. Bias was defined as ERA5 minus ASCAT. Validation statistics included the correlation coefficient (R), bias, root-mean-square error (RMSE), and mean absolute error (MAE). Wind-direction differences were calculated using circular statistics.

To conduct an RMSE-based sensitivity test of the ERA5-based sea-state classification, the wind-speed RMSE obtained from the combined MetOp-B and MetOp-C validation was used as the perturbation amplitude. Three wind-speed scenarios were considered: (U_{10}-RMSE), the baseline ERA5 wind speed (U_{10}), and (U_{10} + RMSE). For each scenario, the inverse wave-age parameter (β_{inv}), the dimensionless wave-height parameter (H^*), and the five sea-state classes were recalculated using the same classification boundaries. Comparisons among the three scenarios were performed using records that remained valid under all perturbations. The resulting class proportions and classification transitions were used to assess the sensitivity of the sea-state classification to wind-speed perturbations of the magnitude indicated by the validation RMSE. In addition, wind–wave directional-difference statistics for the three major sea-state classes were recalculated under all three scenarios using the same common set of valid records to evaluate the robustness of their relative directional characteristics. This analysis is a deterministic, RMSE-based sensitivity test

rather than a full probabilistic uncertainty-propagation analysis; it does not quantify the combined effects of all potential sources of uncertainty.

2.3.3. Statistical Wave Parameters and Joint Occurrence Distribution

Individual waves were identified from the sea-surface displacement records using the zero-upcrossing method. To statistically analyze the wave characteristics, the measured individual wave heights during each recording period were arranged in descending order and denoted as H_1, H_2, H_3, ..., H_n, with the corresponding wave periods denoted as T_1, T_2, T_3, ..., T_n. The mean wave height (H_{mean}) was calculated as the arithmetic mean of all individual wave heights, while the significant wave height ($H_{1/3}$) and one-tenth wave height ($H_{1/10}$) were calculated as the mean heights of the highest one-third and one-tenth of the waves, respectively. The maximum wave height (H_{max}) was defined as the largest individual wave height. The corresponding characteristic periods T_{mean}, $T_{1/3}$, and $T_{1/10}$ were calculated from the periods associated with the respective wave groups, while T_{max} denotes the period associated with H_{max}. These parameters were used to characterize the monthly and overall wave conditions and to evaluate the statistical relationships among different characteristic wave heights and periods.

The joint occurrence distribution of $H_{1/3}$ and $T_{1/3}$ was calculated from all valid observations using bin widths of 0.125 m and 0.25 s, respectively. The conditional mean $H_{1/3}$ was calculated for each $T_{1/3}$ interval when at least 50 observations were available and was lightly smoothed using a three-bin moving average. Occurrence-frequency contours of 0.4%, 0.8%, and 1.2% were superimposed to highlight the principal distribution structure. The number of observations in each bin was divided by the total number of valid records and expressed as occurrence frequency (%).

2.3.4. Wave Spectral Analysis

Wave spectral analysis was performed using a processed sea-surface displacement time series at a sampling frequency of 1.28 Hz. The displacement records were divided into nonoverlapping segments of 256 samples, corresponding to 200 s for each segment. A cosine-shaped window was applied to each segment, with the first and last 32 samples tapered and the remaining samples assigned unit weights. The window coefficients were normalized before applying a 256-point fast Fourier transform (FFT). The resulting spectrum covered the frequency range from 0 to 0.64 Hz, with a frequency resolution of

$$\Delta f = \frac{f_s}{N} = \frac{1.28}{256} = 0.005 \text{ Hz}. \quad (2)$$

where f_s Hz is the sampling frequency and N = 256 is the number of samples used in each FFT segment.

The power spectral density (PSD) obtained for each segment was further smoothed using a three-point weighted average

$$\overline{PSD_l} = \frac{1}{4}PSD_{l-1} + \frac{1}{2}PSD_l + \frac{1}{4}PSD_{l+1} \quad (3)$$

where l denotes the frequency-bin index and PSD_l denotes the smoothed spectral density at the lth frequency bin.

For frequencies $f \leq 0.1$ Hz, all smoothed spectral coefficients were retained, whereas every second coefficient was retained for $f > 0.1$ Hz. Eight consecutive 200 s spectra, covering a total duration of 1600 s, were then arithmetically averaged to obtain the wave spectrum for each half-hourly output cycle, with a new processing cycle initiated every 1800 s.

The resulting spectra were used to examine the temporal evolution of wave spectral density during tropical cyclone events. Changes in spectral density, dominant frequency,

and spectral shape were evaluated using time-frequency distributions and representative spectra before, during, and after the storm passage.

2.3.5. Spectral Peak and Directional Parameters

The primary spectral peak frequency, f_p, was defined as the frequency corresponding to the maximum power spectral density (PSD), and the corresponding spectral density was represented as S_p. Other local maxima in the processed spectrum were subsequently identified, and the local maximum with the largest spectral density, excluding the primary peak, was defined as the strongest secondary peak f_2. Its spectral density was denoted as S_2, and the ratio S_2/S_p was used to quantify the relative strength of the secondary spectral component. To prevent the identification of minor spectral shoulders adjacent to the primary peak as independent secondary peaks, the candidate secondary peaks were required to be separated from f_p by at least 0.02 Hz.

The Datawell SPT files also provide the frequency-dependent mean wave direction and directional spread. For each representative spectrum, the mean wave direction corresponding to the primary spectral peak frequency f_p was represented as D_p, and the directional spread at the same frequency was used to characterize the directional dispersion of the dominant spectral component. Both parameters were obtained directly from the corresponding frequency bins in the SPT output. The wave direction was expressed using the FROM convention, and the directional spread was reported in degrees. Smaller directional spread represents a narrower directional distribution around the mean wave direction.

2.3.6. Wind-Wave and Swell Classification

The observed sea states were classified into wind-wave and swell-related conditions using the dimensionless parameters proposed by Chu et al. [29,30]. In this classification, T_P represents the spectral peak period determined from the peak frequency (f_p) of the wave spectrum ($T_P = 1/f_p$), whereas U_{10} represents the 10 m wind speed obtained from ERA5 reanalysis data. The spectral peak period (T_P) is distinct from the characteristic wave period ($T_{1/3}$) derived from the zero-upcrossing analysis. The peak wavenumber k_p corresponding to T_P was determined from the linear dispersion relation,

$$\left(w_p\right)^2 = g k_p tanh(k_p h) \tag{4}$$

where $w_p = 2\pi/T_P$ is the angular frequency at the spectral peak, g is the gravitational acceleration, and h is the local water depth. The phase velocity corresponding to the spectral peak was then calculated as follows:

$$c_p = \left(\frac{w_p}{k_p}\right) \tag{5}$$

Using $H_{1/3}$, U_{10}, and C_p, the dimensionless parameters used for sea-state classification were calculated as follows:

$$H^* = \frac{1}{16}\left(\frac{gH_{1/3}}{U_{10}^2}\right)^2, \beta_{inv} = \frac{U_{10}}{C_p} \tag{6}$$

where $H_{1/3}$ is the significant wave height, H^* is the dimensionless wave-height parameter, and β_{inv} is the inverse wave-age parameter. Based on these parameters, the observed sea states were classified as pure wind waves, wind-dominated mixed waves, swell-dominated mixed waves, pure swell, and overdeveloped wind waves. Following Chu et al. [29,30], the classification boundaries were $H^* = 1$, $H^* = 3.64 \times 10^{-3}$, and $\beta_{\mathrm{inv}} = 0.82$.

Importantly, this classification is not based solely on the characteristic wave period. It combines the observed spectral peak period and significant wave height with ERA5 10 m

wind speed through the inverse wave-age parameter ($\beta_{inv} = U_{10}/C_P$) and the dimensionless wave-height parameter (H^*). The inverse wave-age parameter describes the relationship between local wind speed and the phase speed of the dominant waves, while H^* provides an additional constraint on the sea state. These two parameters are jointly used to distinguish wind-wave-dominated, swell-dominated, and mixed conditions according to the prescribed classification thresholds. The resulting categories represent bulk sea-state classifications rather than a direct spectral separation of wind-sea and swell energy.

3. Results and Discussion

3.1. Overall Wave Environment

The observed wave conditions exhibited pronounced temporal variability during the measurement period from December 2023 to August 2024. Figure 3a,b shows the full time series of buoy-observed significant wave height ($H_{1/3}$), characteristic wave period ($T_{1/3}$), and mean wave period T_{mean}, together with ERA5 significant wave height (SWH) and mean wave period (MWP), during the nine-month observation period. Specifically, Figure 3a compares buoy-observed $H_{1/3}$ with ERA5 SWH, whereas Figure 3b presents buoy-observed $T_{1/3}$ and T_{mean} alongside ERA5 MWP. The buoy-derived T_{mean} series is included to illustrate the observed temporal variability in mean wave period, while the quantitative ERA5 wave-period comparison is based on $T_{1/3}$ and MWP. ERA5 reproduced the temporal evolution of significant wave height particularly well. Based on 6307 temporally matched records, the comparison between buoy $H_{1/3}$ and ERA5 SWH yielded a correlation coefficient of (R = 0.941), a bias of (0.062 m), an RMSE of (0.257 m), and an MAE of (0.194 m). The small positive bias indicates a slight overall overestimation of significant wave height by ERA5.

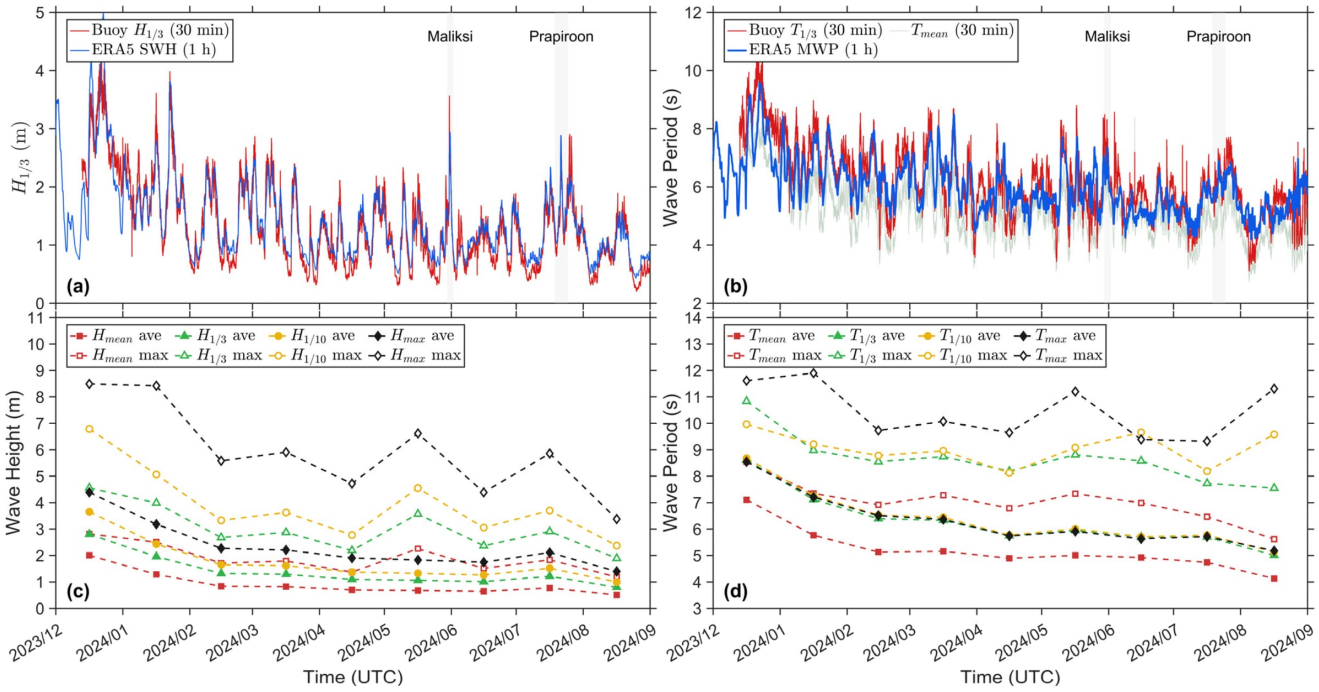


Figure 3. Temporal variations in wave conditions during the observation period from December 2023 to August 2024: (**a**) buoy-observed significant wave height ($H_{1/3}$) and ERA5 significant wave height (SWH); (**b**) buoy-observed characteristic wave period ($T_{1/3}$), buoy-observed mean wave period (T_{mean}), and ERA5 mean wave period (MWP); (**c**) monthly wave-height statistics; and (**d**) monthly wave-period statistics. Shaded intervals in panels (**a**,**b**) indicate the passage periods of Tropical Storm Maliksi and Severe Tropical Storm Prapiroon.

The wave-period comparison also showed good temporal consistency, although the agreement was weaker than that for significant wave height. For 6307 temporally matched records, buoy ($T_{1/3}$) and ERA5 mean wave period (MWP) yielded (R = 0.820), a bias of (-0.188) s, an RMSE of 0.726 s, and an MAE of 0.557 s. The negative bias indicates that ERA5 MWP was, on average, slightly shorter than the observed ($T_{1/3}$). Because the two period parameters are derived using different definitions, this comparison is interpreted as an assessment of their temporal consistency rather than a strict like-for-like validation. The monthly mean significant wave height ($H_{1/3}$) ranged from approximately 0.80 to 2.81 m, with an average of 1.40 m across the nine monthly means (Table 1). Higher wave conditions typically occurred during the early part of the observation period, particularly in December and January, whereas relatively lower wave heights were observed during spring and summer. The lowest mean monthly $H_{1/3}$ values were observed in August. A similar temporal pattern was observed for the mean wave height (H_{mean}), one-tenth of the wave height ($H_{1/10}$), and maximum wave height (H_{max}).

Table 1. Monthly statistics of observed Wave parameters.

Monthly Parameter	Month 2023	Month 2024								Mean Across Months	Maximum Across Months
	Dec	Jan	Feb	Mar	Apr	May	Jun	Jul	Aug		
T_p average (s)	8.61	8.10	7.35	7.27	6.29	6.86	6.25	6.48	6.07	7.03	8.61
T_p maximum (s)	10.84	11.11	11.11	15.38	11.11	13.33	10.00	10.53	12.50	11.77	15.38
H_{mean} average (m)	2.00	1.29	0.84	0.82	0.70	0.68	0.65	0.77	0.51	0.92	2.00
H_{mean} maximum (m)	2.82	2.51	1.71	1.79	1.37	2.26	1.51	1.84	1.19	1.89	2.82
$H_{1/3}$ average (m)	2.81	1.96	1.32	1.29	1.10	1.06	1.01	1.22	0.80	1.40	2.81
$H_{1/3}$ maximum (m)	4.56	3.99	2.68	2.87	2.19	3.57	2.37	2.91	1.90	3.00	4.56
$H_{1/10}$ average (m)	3.66	2.44	1.65	1.62	1.37	1.33	1.27	1.52	1.00	1.76	3.66
$H_{1/10}$ maximum (m)	6.79	5.07	3.33	3.63	2.77	4.55	3.06	3.70	2.38	3.92	6.79
H_{max} average (m)	4.39	3.18	2.28	2.21	1.91	1.83	1.75	2.11	1.40	2.34	4.39
H_{max} maximum (m)	8.49	8.42	5.58	5.91	4.72	6.62	4.39	5.86	3.38	5.93	8.49
T_{mean} average (s)	7.11	5.77	5.13	5.16	4.89	5.01	4.92	4.74	4.13	5.21	7.11
T_{mean} maximum (s)	8.55	7.35	6.92	7.28	6.79	7.34	6.99	6.47	5.62	7.03	8.55
$T_{1/3}$ average (s)	8.61	7.12	6.40	6.33	5.74	5.95	5.70	5.71	5.01	6.29	8.61
$T_{1/3}$ maximum (s)	10.84	8.98	8.55	8.74	8.19	8.81	8.58	7.73	7.55	8.66	10.84
$T_{1/10}$ average (s)	8.68	7.26	6.53	6.44	5.77	6.01	5.71	5.77	5.14	6.37	8.68
$T_{1/10}$ maximum (s)	9.96	9.21	8.78	8.96	8.13	9.08	9.66	8.19	9.58	9.06	9.96
T_{max} average (s)	8.55	7.21	6.51	6.37	5.74	5.91	5.63	5.72	5.18	6.31	8.55
T_{max} maximum (s)	11.61	11.90	9.73	10.07	9.65	11.20	9.39	9.32	11.31	10.46	11.90

Wave periods also showed distinct monthly variations. The mean monthly significant wave period ($T_{1/3}$) ranged from approximately 5.01 to 8.61 s, and the mean of the monthly mean values was 6.29 s. Longer wave periods occurred predominantly during December and January, whereas shorter periods were typically observed from late spring to summer. The variations in Tmean, $T_{1/3}$, $T_{1/10}$, and T_{max} exhibited overall consistency, indicating that changes in wave height were associated with corresponding variations in the wave period during the observation period.

Figure 4 shows the joint occurrence distribution of $H_{1/3}$ and $T_{1/3}$ during the deployment period. The observations were concentrated primarily within moderate wave conditions, with the highest occurrence frequency corresponding to an $H_{1/3}$ of approximately 1.12 m and a $T_{1/3}$ of approximately 5.75 s. Most frequently occurring sea states were distributed approximately within $H_{1/3}$ = 0.5–2.0 m and $T_{1/3}$ = 4.5–7.0 s, whereas combinations of large wave heights and long periods occurred notably less frequently. The conditional-mean curve showed a systematic increase in $H_{1/3}$ with increasing $T_{1/3}$, indicating that longer-period conditions were generally associated with larger significant wave heights.

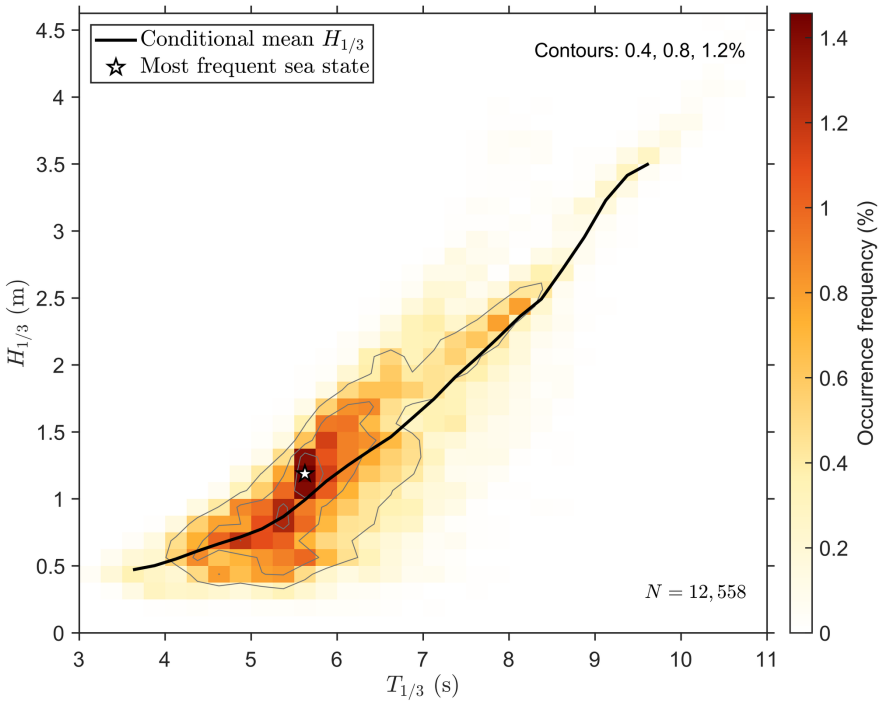


Figure 4. Joint occurrence distribution of significant wave height ($H_{1/3}$) and significant wave period ($T_{1/3}$) during the observation period. Colors indicate the occurrence frequency within each (0.125)-m × (0.25)-s bin. The gray contours denote occurrence frequencies of 0.4%, 0.8%, and 1.2%. The solid black curve represents the conditional mean ($H_{1/3}$) for each ($T_{1/3}$) interval, and the star marks the most frequently occurring sea state.

Figure 5 shows a comparison of overall directional distributions of the observed waves and ERA5 10 m winds during the observation period. The observed wave field exhibited a pronounced directional preference, with waves from the east northeast and eastern sectors occurring most frequently. ENE and E waves accounted for approximately 25.6% and 18.8% of observations, respectively. The wind field also exhibited a distinct directional distribution, although the relationship between the local wind and wave directions varied among the different sea-state conditions. Therefore, the overall directional relationship was further examined using wind-wave and swell classification and the corresponding wind–wave directional differences.

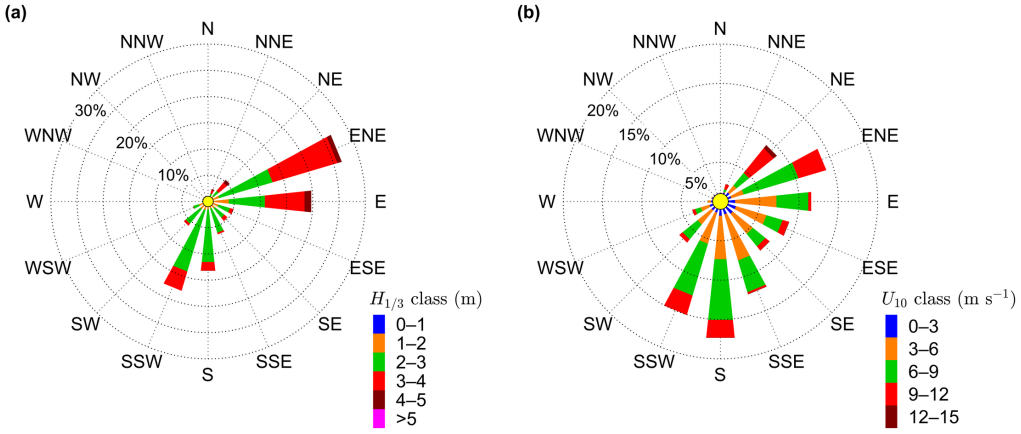


Figure 5. Comparison of overall directional distributions during the observation period: (**a**) observed wave-direction rose and (**b**) ERA5 10 m wind-direction rose.

To evaluate the reliability of the ERA5 winds used in the wind–wave classification, ERA5 10 m winds were compared with collocated MetOp-B and MetOp-C ASCAT observations. A total of 474 valid matchups were obtained. The combined comparison showed good agreement in wind speed, with (R = 0.924), a bias of −0.191 m s^{-1}, an RMSE of 1.066 m s^{-1}, and an MAE of 0.809 m s^{-1}. The corresponding mean ASCAT and ERA5 wind speeds were 6.980 and 6.789 m s^{-1}, respectively. Wind direction also showed generally good agreement, with a circular bias of 2.42°, an MAE of 10.49°, and 89.0% and 97.7% of the matchups falling within 22.5° and 45°, respectively. The ERA5–ASCAT comparison and detailed validation statistics are presented in Figure S1 and Table S1, respectively.

Using the baseline ERA5 winds and the common valid records, swell-dominated mixed seas represented the largest sea-state category, accounting for 58.0% of the observations, followed by pure wind seas (23.4%) and wind-dominated mixed seas (16.8%). However, the classification exhibited substantial sensitivity to systematic perturbations of (U_{10}) by the ASCAT-derived RMSE of 1.066 m s^{-1}). Under the (U_{10}-RMSE) scenario, the proportion of swell-dominated mixed seas increased to 77.7%, whereas pure wind seas and wind-dominated mixed seas decreased to 8.4% and 7.1%, respectively. In contrast, under the (U_{10} + RMSE) scenario, swell-dominated mixed seas decreased to 34.1%, while pure wind seas and wind-dominated mixed seas increased to 39.6% and 25.9%, respectively, with pure wind seas becoming the most frequent category. Pure swell and overdeveloped wind-wave conditions remained comparatively uncommon.

This sensitivity arises directly from the dependence of the classification parameters on wind speed: (β_{inv}) varies linearly with (U_{10}), whereas (H^*) varies approximately as ($U_{10}{}^{-4}$). Consequently, an increase in (U_{10}) shifts the observations toward larger (β_{inv}) and substantially smaller (H^*), causing many records to cross the classification boundaries toward wind-sea-dominated categories. Conversely, decreasing (U_{10}) shifts the classification toward swell-dominated conditions. The baseline ERA5 classification therefore indicates a substantial contribution from swell-dominated mixed seas, but the exact class proportions—and under the U_{10} + RMSE scenario, even the identity of the most frequent class—are sensitive to uncertainty in (U_{10}). Accordingly, the sea-state percentages should be interpreted as an ERA5-dependent diagnostic rather than as uncertainty-free climatological fractions. The ±RMSE scenarios are intended to assess the sensitivity of the classification to wind-speed perturbations of a magnitude consistent with the validation error, rather than to provide probabilistic confidence intervals for the estimated class proportions. Other potential sources of uncertainty, including spatial and temporal representativeness and uncertainties in the wave parameters, were not jointly propagated in this analysis. The baseline classification and its response to the ±1 RMSE wind-speed perturbations are summarized in Figure 6. The detailed sea-state proportions under the three wind-speed scenarios are summarized in Table S2.

To further examine the directional relationship between local winds and waves, the absolute directional difference, $|\Delta\theta|$, between the ERA5 10 m wind direction and the observed wave direction was analyzed for the three major sea-state classes (Figure 7). The pure wind seas exhibited the strongest wind–wave directional agreement with the smallest median directional difference and a relatively narrow interquartile range. More than 70% of the pure wind-sea observations showed directional differences within 22.5°, and approximately 97% were within 45°. In contrast, both wind-dominated and swell-dominated mixed seas showed broader directional difference distributions, with only 44–45% of the observations within 22.5°. The proportion of cases with directional differences ≥ 45° also increased under mixed-sea conditions, particularly in swell-dominated mixed seas. The cumulative distributions further confirmed this contrast, with approximately 75–77% of wind-dominated mixed-sea observations and 70–73% of swell-dominated mixed-sea observations remaining within 45°.

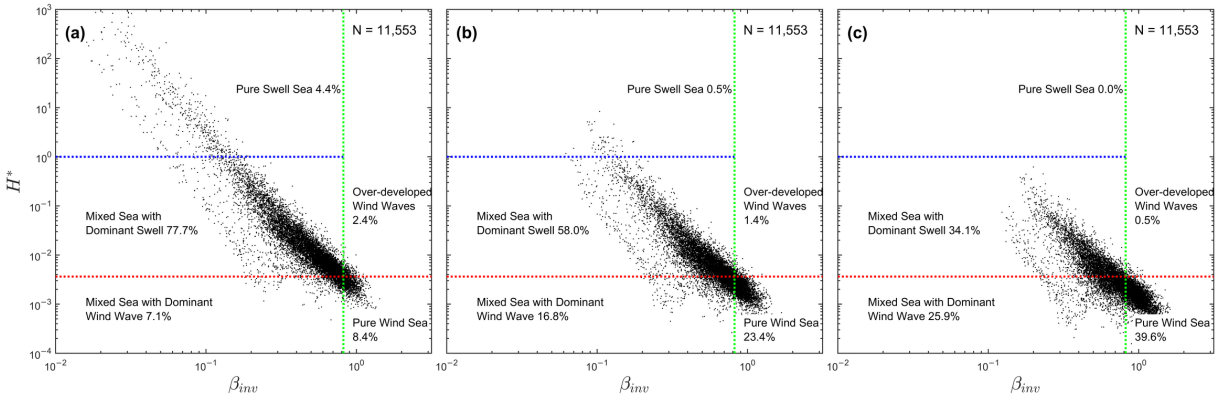


Figure 6. Sensitivity of the wind-wave and swell classification to ERA5 wind-speed uncertainty: (**a**) U_{10} RMSE, (**b**) baseline ERA5 U_{10}, and (**c**) U_{10} + RMSE, where RMSE = 1.066 m s^{-1} was obtained from the combined ASCAT–ERA5 validation. All panels use the same classification thresholds and common valid records.The green vertical dotted line indicates the threshold $\beta_{\text{inv}} \leq 0.82 = 0.82$, the red horizontal dotted line indicates $H^* = 3.64 \times 10^{-3}$, and the blue horizontal dotted line indicates $H^* = 1$ for $\beta_{\text{inv}} \leq 0.82$. These lines represent the thresholds used for sea-state classification.

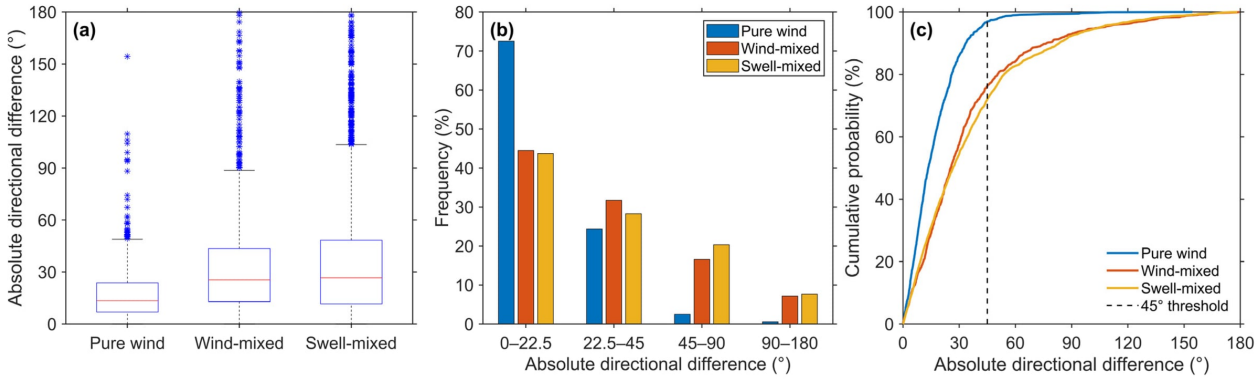


Figure 7. Wind–wave directional differences for pure wind seas, wind-dominated mixed seas, and swell-dominated mixed seas: (**a**) box plots of absolute directional differences; (**b**) frequency distributions; and (**c**) cumulative probability distributions. In panel (**a**), asterisks indicate outliers beyond the whiskers, defined as observations below Q1 − 1.5 × IQR or above Q3 + 1.5 × IQR, where IQR is the interquartile range.

The broader distribution of wind–wave directional differences under swell-dominated mixed-sea conditions was consistent with the increased influence of swell components, whose directions were not consistent with the contemporaneous local winds. However, most mixed-sea observations exhibited absolute wind-wave directional differences of 45°or less, suggesting that the observed wave directions were often broadly aligned with the contemporaneous local winds. Nevertheless, directional agreement alone does not quantify the relative energy contributions of locally generated wind waves and remotely generated swell.

The sensitivity analysis further showed that, although the sea-state proportions varied with the ERA5 wind-speed perturbations, the relative wind–wave directional characteristics remained consistent. Pure wind seas retained the smallest median absolute directional differences (12.6–15.1°) across the (U_{10}-RMSE), baseline, and (U_{10} + RMSE) scenarios, compared with 20.0–29.4° for wind-dominated mixed seas and 23.4–31.2° for swell-dominated mixed seas. In addition, 68.4–75.5% of pure wind-sea cases remained within 22.5°, and 95.2–97.1% remained within 45°, robust. Detailed wind–wave consistently exceeded the corresponding proportions for both mixed-sea classes. Thus, while the quantitative sea-state partition was sensitive to (U_{10}), the stronger wind–wave directional agreement under pure

wind-sea conditions remained qualitatively directional-difference statistics for the three major sea-state classes under all three wind-speed scenarios are provided in Table S3.

The wind–wave directional relationship observed east of Hainan Island differed from that reported for the eastern Guangdong offshore waters by Liu et al. [31], where the dominant wind and wave sectors were both concentrated primarily in the northeastern–eastern directions. The two sites also differed substantially in their sea-state composition. Under the baseline ERA5-based classification, the present site showed a larger fraction of swell-dominated mixed seas (58%) than that reported by Liu et al. [31] (37.8%). However, the sensitivity experiments demonstrated that the exact class proportions depend appreciably on the wind speed used in the classification. Therefore, quantitative differences between the two sites should be interpreted with caution because they may reflect not only differences in site exposure, water depth, and wave climate, but also differences in the representation of local wind forcing.

The directional distributions, sea-state classifications, and wind–wave directional differences exhibited contributions from both local wind forcing and remotely generated swells to the background wave field east of Hainan Island. The tropical-cyclone-induced response is examined separately in Section 3.3.

3.2. Statistical Characteristics of Wave Parameters

The linear relationships among the different characteristic wave heights were examined using linear regression. As shown in Figure 8a–c, the fitted regression slopes for $H_{1/3}$ versus H_{mean}, $H_{1/10}$ versus $H_{1/3}$, and H_{max} versus $H_{1/3}$ were 1.586, 1.249, and 1.695, respectively, with relatively small intercepts of −0.011 m, approximately 0 m, and 0.034 m. For comparison, the corresponding coefficients reported by Longuet-Higgins [32] were 1.598, 1.271, and 1.628; those reported by Gao et al. [33] were 1.530, 1.229, and 1.655; and those reported by Liu et al. [31] were 1.512, 1.229, and 1.487, respectively. The present coefficients were generally within the range of previously reported values, with the largest difference occurring in the H_{max}–$H_{1/3}$ relationship.

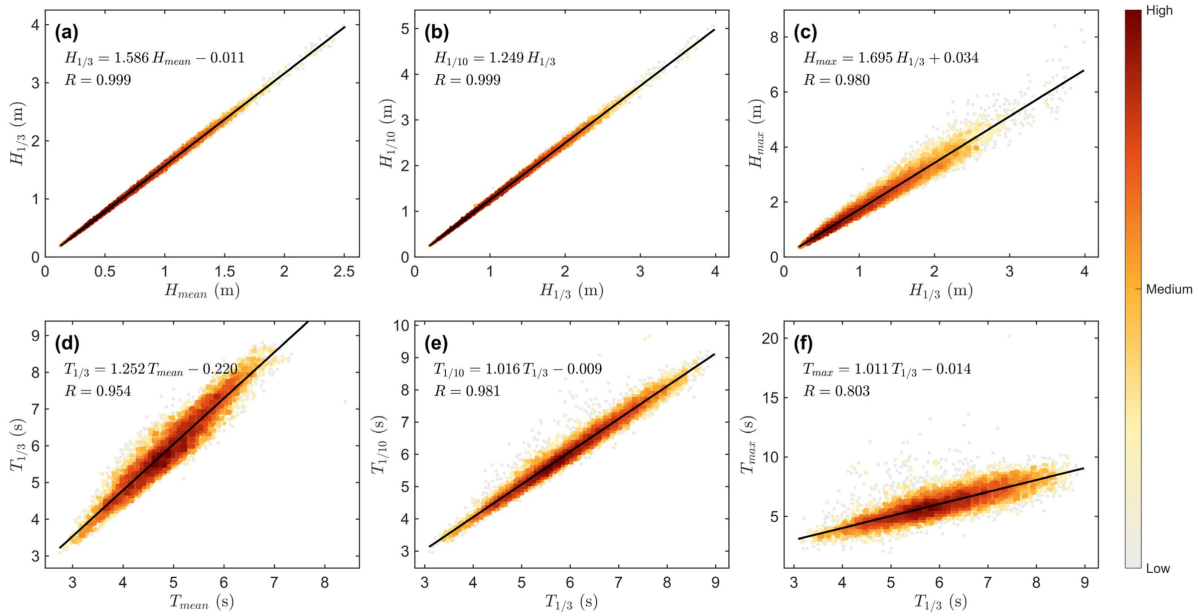


Figure 8. Density distributions and linear regression relationships among characteristic wave parameters: (**a**) $H_{1/3}$ versus H_{mean}; (**b**) $H_{1/10}$ versus $H_{1/3}$; (**c**) H_{max} versus $H_{1/3}$; (**d**) $T_{1/3}$ versus T_{mean}; (**e**) $T_{1/10}$ versus $T_{1/3}$; and (**f**) Tmax versus $T_{1/3}$. Point color indicates relative local observation density, and solid black lines represent linear regression fits.

Linear relationships among the characteristic wave periods were also identified. Figure 8d–f shows the relationships between $T_{1/3}$ and T_{mean}, $T_{1/10}$ and $T_{1/3}$, and T_{max} and $T_{1/3}$. The fitted regression slopes were 1.252, 1.016, and 1.011, with correlation coefficients of 0.954, 0.981, and 0.803. Among these relationships, T_{max} showed the greatest scatter relative to $T_{1/3}$ ($R = 0.803$), indicating a substantially larger variability in the period associated with individual maximum waves than in the bulk characteristic wave periods.

Table 2 presents a comparison of these wave-period relationship coefficients with values reported for Xiangshui, Chiwan, the Japanese coast, Shijiu, Lianyungang, eastern Guangdong, and other coastal regions. The eastern Hainan coefficients were within the range reported for other sea areas, whereas the interregional differences revealed that these wave-period relationships were not spatially uniform (Table 2).

Table 2. Comparison of characteristic wave-period relationship coefficients in different sea areas.

Relationship	Gao et al. [33]	Yang et al. [34]	Goda and Nagai [35]	Yu and Liu [36]	Ge [37]	Liu et al. [31]	This Study
$T_{1/3}$ vs. T_{mean}	1.320	1.09	1.1–1.3	1.18	1.35	1.121	1.252
$T_{1/10}$ vs. $T_{1/3}$	1.133	1.03	1	1	1.15	1.004	1.016
T_{max} vs. $T_{1/3}$	–	–	1	1	–	1.001	1.011
Position	Xiangshui	Chiwan	Japanese Coast	Shijiu	Lianyungang	Eastern Guangdong	Eastern Hainan

Note: Values for this study represent slopes obtained from linear regressions with a free intercept.

3.3. Wave and Spectral Evolution During Tropical Cyclone Events

Two tropical cyclone events affected the study region during the observation period: tropical storm Maliksi and severe tropical storm Prapiroon. The durations and corresponding wave characteristics are presented in Tables 3 and 4, respectively. As shown in Figure 1, Maliksi passed considerably closer to the observation site, whereas Prapiroon followed a more westward track toward Hainan Island. Although Prapiroon reached a higher maximum intensity category, Maliksi passed considerably closer to the observation site (51.7 km versus 238.2 km) and generated the stronger local wave response. This contrast suggests that the observed wave response was influenced by the maximum cyclone intensity, as well as by the storm track and its proximity to the observation site. Maliksi produced a stronger wave response than that of Prapiroon, with mean $H_{1/3}$ values of 2.06 and 1.49 m, maximum individual wave heights of 6.62 and 5.19 m, and mean $T_{1/3}$ values of 7.31 and 6.19 s, respectively (Table 4). Overall, Maliksi was characterized by higher waves and generally longer characteristic periods.

Table 3. Characteristics of the two tropical cyclones affecting the study region during the observation period.

Tropical Cyclone	Period (UTC)	Maximum Sustained Wind Speed ($m\ s^{-1}$)	Closest Distance (km)
Maliksi	30 May–1 June 2024	24.4	51.7
Prapiroon	19 July–24 July 2024	32.6	238.2

Table 4. Wave-height and wave-period responses during Maliksi and Prapiroon.

Tropical Cyclone	Statistic	$H_{1/3}$ (m)	$H_{1/10}$ (m)	H_{max} (m)	$T_{1/3}$ (s)	$T_{1/10}$ (s)	T_{max} (s)
Maliksi	mean	2.06	2.57	3.54	7.31	7.32	7.12
	range	1.32–3.57	1.60–4.55	1.97–6.62	6.49–8.33	6.25–8.35	5.25–8.91
Prapiroon	mean	1.49	1.86	2.58	6.19	6.31	6.21
	range	0.80–2.69	0.99–3.35	1.30–5.19	4.96–7.33	5.05–7.61	4.39–8.67

Therefore, Maliksi was selected for the detailed time-series and spectral evolution analyses presented below. Figure 9 shows the temporal evolution of ERA5 wind forcing and the observed wave parameters during the event. As Maliksi approached the observation site, the local wind field intensified and rotated notably, followed by an increase in the observed wave heights and a pronounced change in wave direction. The characteristic wave periods also varied during the storm passage. After the storm moved away from the observation region, the wave heights gradually decreased toward their pre-storm levels.

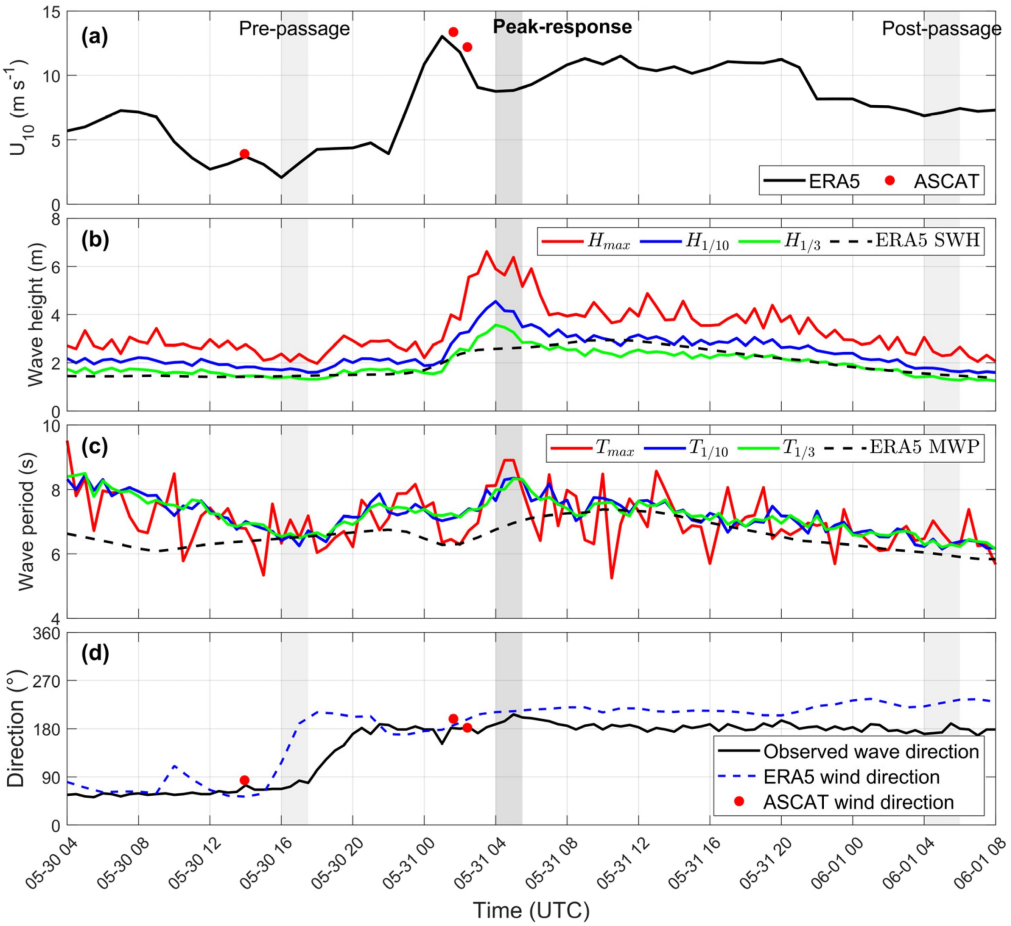


Figure 9. Temporal variations in ERA5 wind forcing and observed wave parameters during Tropical Storm Maliksi: (**a**) ERA5 10 m wind speed U_{10} and ASCAT-retrieved wind speed; (**b**) characteristic wave heights and ERA5 significant wave height (SWH); (**c**) characteristic wave periods and ERA5 mean wave period (MWP); and (**d**) ERA5 wind direction, observed wave direction, and ASCAT-retrieved wind direction. Shaded intervals indicate the representative pre-passage, peak-response, and post-passage spectral windows used in Table 5.

To evaluate the consistency of the ERA5 wave parameters during Tropical Storm Maliksi, the ERA5 significant wave height (SWH) and mean wave period (MWP) were compared with the buoy-derived significant wave height $H_{1/3}$ and characteristic wave period $T_{1/3}$, respectively (Figure 9b,c). For 53 matched records, ERA5 SWH showed good agreement with the observed $H_{1/3}$, with a correlation coefficient of 0.848, a bias of 0.016 m, an RMSE of 0.299 m, and an MAE of 0.220 m. The small positive bias indicates that ERA5 slightly overestimated wave height on average, while the relatively high correlation suggests that it captured the main temporal variations in wave height during the event. The agreement was weaker for the wave-period comparison, with a correlation coefficient of 0.433, a bias of −0.630 s, an RMSE of 0.831 s, and an MAE of 0.636 s. ERA5 MWP was shorter than the buoy-derived $T_{1/3}$ on average; however, this difference should be inter-

preted cautiously because the two period parameters are derived using different definitions. Accordingly, their comparison is used to assess temporal consistency rather than strict parameter-equivalent accuracy.

Table 5. Frequency and directional spectral characteristics of representative wave spectra before, during, and after Tropical Storm Maliksi.

Stage	Time (UTC)	f_p (Hz)	S_p (m² Hz^{-1})	D_p (°)	Directional Spread (°)	f_2 (Hz)	S_2 (m² Hz^{-1})	S_2/S_p
Pre-passage	30 May 16:00	0.120	2.080	67.5	24.2	0.160	1.354	0.651
	30 May 17:00	0.130	1.872	83.0	47.9	0.170	1.685	0.900
	30 May 17:30	0.120	1.845	78.8	40.6	0.180	1.225	0.664
Peak-response	31 May 04:00	0.120	17.413	188.4	29.8	0.190	2.438	0.140
	31 May 04:30	0.120	20.332	194.1	29.2	0.170	3.355	0.165
	31 May 05:30	0.100	20.029	201.1	17.9	0.260	0.421	0.021
Post-passage	1 June 04:00	0.140	1.891	170.2	44.4	0.120	1.668	0.882
	1 June 05:00	0.140	2.591	173.0	34.4	0.220	0.619	0.239
	1 June 06:00	0.130	1.480	180.0	40.1	0.160	1.450	0.980

Note: f_p and S_p represent the frequency and spectral density of the primary spectral peak, respectively; D_p and directional spread represent the mean wave direction and directional spread at f_p, respectively. f_2 and S_2 represent the frequency and spectral density of the strongest secondary spectral peak, respectively, and S_2/S_p represents the secondary-to-primary peak spectral-density ratio. Wave directions follow the FROM convention.

To further evaluate the performance of ERA5 wave parameters during tropical cyclone events, an additional comparison was conducted for Severe Tropical Storm Prapiroon using the same temporal matching procedure and statistical metrics as those applied to Maliksi. For 140 matched records, the comparison between buoy-observed significant wave height ($H_{1/3}$) and ERA5 significant wave height (SWH) yielded a correlation coefficient of 0.946, a bias of 0.132 m, an RMSE of 0.201 m, and an MAE of 0.177 m. The corresponding comparison between buoy-observed characteristic wave period ($T_{1/3}$) and ERA5 mean wave period (MWP) yielded a correlation coefficient of 0.775, a bias of −0.143 s, an RMSE of 0.373 s, and an MAE of 0.303 s.

Compared with Maliksi, the Prapiroon event exhibited higher correlation coefficients and lower RMSE and MAE values for both wave height and wave period, although the positive mean bias in significant wave height was larger. These results indicate that the agreement between ERA5 and buoy observations varied between the two tropical cyclone events. Because buoy-derived $T_{1/3}$ and ERA5 MWP are defined differently, the wave-period comparison is interpreted as an assessment of temporal consistency rather than strict parameter-equivalent accuracy. The evaluation statistics for both events are summarized in Table S4.

For the detailed analysis of Maliksi, three quality-controlled ASCAT wind retrievals were available during the comparison period (30 May 2024 04:00–1 June 2024 08:00 UTC), including two from MetOp-B and one from MetOp-C. The distances between these retrieval locations and the buoy were 2.92–17.18 km, with a mean distance of 8.35 km. The ASCAT observations provide independent snapshots of wind speed and direction for comparison with ERA5 (Figure 9a,d). Although the available retrievals were broadly consistent with ERA5 at the satellite overpass times, their sparse temporal sampling limits their ability to validate the continuous evolution of the storm-time wind field. Therefore, ERA5 provides the continuous temporal context for the event, while ASCAT serves as an independent observational cross-check.

The corresponding evolution of the wave spectral density is shown in Figure 10. Spectral density increased substantially during the cyclone passage, particularly within the frequency range of approximately 0.02–0.20 Hz. The strongest enhancement occurred at

approximately 0.10–0.12 Hz during the peak-response stage, when the maximum spectral density reached approximately 20.3 m^2 Hz^{-1}. Compared to the pre-storm spectra, this represents an approximately tenfold increase in the peak spectral density.

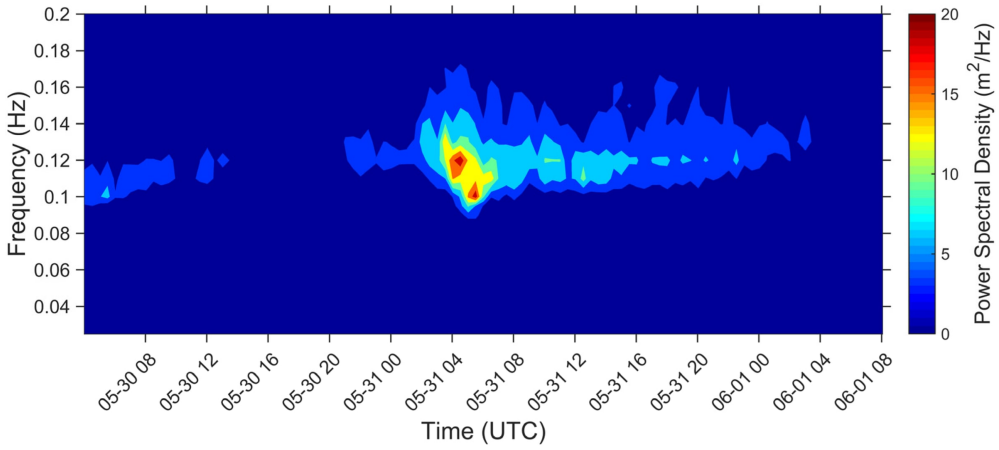


Figure 10. Time frequency evolution of wave power spectral density during Tropical Storm Maliksi.

The representative spectra from the pre-passage, peak-response, and post-passage stages are shown in Figure 11, and their associated frequency and directional spectral parameters are presented in Table 5. Prior to the strongest cyclone influence, the spectra exhibited a distinct multi-component structure. The primary spectral peaks occurred at approximately 0.12–0.13 Hz, whereas secondary peaks occurred at approximately 0.16–0.18 Hz. The secondary peaks retained approximately 65–90% of the spectral density of the corresponding primary peaks, indicating a pronounced double-peaked spectral structure. The mean wave direction associated with the primary spectral peaks ranged from 67.5° to 83.0° with directional spreads of 24.2–47.9°.

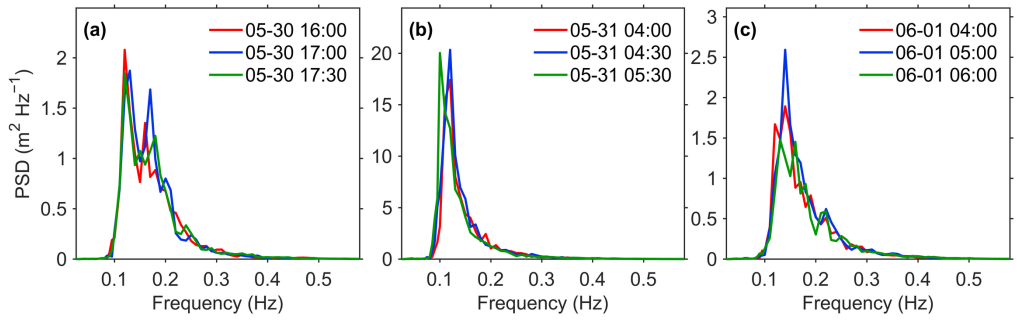


Figure 11. Representative wave spectra during (**a**) the pre-passage stage, (**b**) the peak-response stage, and (**c**) the post-passage stage of Tropical Storm Maliksi.

During the peak-response stage, the spectral structure changed significantly. The dominant peak became concentrated at approximately 0.10–0.12 Hz, while the maximum spectral density increased to 17.4–20.3 m^2Hz^{-1}. Simultaneously, the mean direction associated with the dominant spectral peak shifted to approximately 188.4–201.1°, and the corresponding directional spread decreased to 17.9–29.8°. The secondary spectral peaks became much weaker, with secondary-to-primary peak ratios typically <0.17. During the strongest storm influence, the initially multi-component wave field was therefore dominated by a considerably stronger and more directionally concentrated spectral component.

Following the storm passage, spectral density decreased notably, with maximum values returning to approximately 1.48–2.59 m^2 Hz^{-1}. The dominant spectral peaks were located mainly at 0.13–0.14 Hz, with corresponding mean directions of approximately 170.2–180.0°.

Directional spreads subsequently increased to approximately 34.4–44.4°, indicating a reduction in the directional concentration. In addition, relatively strong secondary peaks appeared in certain post-passage spectra. In particular, the secondary-to-primary peak ratios reached approximately 0.88 and 0.98 in two of the three representative records, suggesting a partial re-establishment of a multi-component spectral structure with a reduction in the influence of the cyclone.

The spectral evolution broadly corresponded to changes in local wind forcing. As Maliksi approached the observation site, ERA5 U_{10} increased rapidly, followed by an increase in the observed wave heights and a strong spectral density enhancement at approximately 0.10–0.12 Hz. The rapid intensification of the local wind forcing was observed several hours before the strongest wave response. During the subsequent peak-response stage, the primary spectral peak notably strengthened, whereas the secondary-to-primary peak ratio substantially decreased. The simultaneous strengthening of the primary peak and reduction in S2/Sp coincided with the period of enhanced cyclone-related wind forcing. After the storm passed, both wind forcing and spectral density weakened, and the secondary spectral components became relatively more pronounced again.

Therefore, Maliksi transformed the initially weak, multi-component wave field into a transient high-energy state dominated by a directionally concentrated spectral component, and secondary components re-emerged as the storm influence weakened.

4. Conclusions

This study analyzed nine months of directional wave observations east of Hainan Island to characterize the regional wave environment, statistical relationships among wave parameters, and tropical cyclone-induced spectral evolution. The main conclusions are as follows:

(1) The observed wave environment exhibited clear temporal and directional variability. The monthly mean ($H_{1/3}$) ranged from 0.80 to 2.81 m and ($T_{1/3}$) from 5.01 to 8.61 s, with ENE and E waves occurring predominantly. The baseline ERA5-based classification indicated a predominance of swell-dominated mixed seas, although the exact class proportions were sensitive to ±1 RMSE perturbations of (U_{10}). Nevertheless, the relative wind–wave directional characteristics remained robust: pure wind seas consistently exhibited the strongest directional agreement across all sensitivity scenarios, with the smallest median directional differences and the largest fractions of cases within 22.5° and 45°. These findings are based on an RMSE-based sensitivity test and should not be interpreted as a complete quantification of the uncertainty in the sea-state classification.

(2) Site-specific empirical linear relationships were identified among the characteristic wave parameters. The fitted regression slopes for $H_{1/3}$ versus Hmean, $H_{1/10}$ versus $H_{1/3}$, and Hmax versus $H_{1/3}$ were 1.586, 1.249, and 1.695, respectively, whereas the corresponding wave-period slopes were 1.252, 1.016, and 1.011, respectively. These coefficients characterize the empirical relationships among the wave parameters at the offshore observation site east of Hainan Island during the nine-month deployment.

(3) Tropical Storm Maliksi generated a stronger wave response than Prapiroon. During Maliksi, the mean $H_{1/3}$ was 2.06 m and the maximum individual wave height was 6.62 m, compared with 1.49 m and 5.19 m during Prapiroon. Spectral density increased markedly at approximately 0.10–0.12 Hz during Maliksi, and the pre-storm multi-component spectral structure evolved into a more concentrated dominant wave system during the peak response stage. The mean wave direction associated with the dominant spectral peak underwent a pronounced shift, whereas its directional spread decreased during the strongest storm influence and increased again after the storm

passed. The Maliksi observations showed concurrent changes in bulk wave parameters, spectral structure, and the directionality of the dominant spectral component under tropical-cyclone forcing.

Several limitations should be acknowledged. First, the observations cover only nine months, from December 2023 to August 2024, and therefore do not represent a complete annual cycle or the interannual variability of the regional wave climate. Second, the measurements were obtained from a single offshore buoy at a water depth of approximately 120 m east of Hainan Island. Consequently, the reported wave statistics, sea-state proportions, and tropical cyclone responses primarily characterize the local conditions during the observation period and should not be generalized to the entire northern South China Sea without further validation. In addition, the ERA5-based sea-state proportions are sensitive to wind-speed perturbations, as demonstrated by the RMSE-based sensitivity test. Longer-term observations from multiple stations would be valuable for assessing the spatial representativeness and temporal variability of these findings.

Supplementary Materials: The following supporting information can be downloaded at https://www.mdpi.com/article/10.3390/jmse14212027/s1: Figure S1: Validation of ERA5 10-m winds against spatially and temporally matched MetOp-B and MetOp-C ASCAT observations; Table S1: ERA5–ASCAT wind validation statistics; Table S2: Sea-state classification sensitivity under the U_{10} − RMSE, baseline U_{10}, and U_{10} + RMSE scenarios; Table S3: Wind–wave directional-difference statistics for the three major sea-state classes under the U_{10} − RMSE, baseline U_{10}, and U_{10} + RMSE scenarios; Table S4: Event-specific comparison statistics for buoy-observed and ERA5 wave parameters during Tropical Storm Maliksi and Severe Tropical Storm Prapiroon.

Author Contributions: Conceptualization, Y.M.; methodology, X.N.; software, Y.M.; formal analysis, Y.M.; investigation, D.Z. and F.L.; data curation, Y.M.; writing—original draft preparation, Y.M.; writing—review and editing, X.Z. and X.N.; visualization, Y.M.; supervision, X.Z.; project administration, X.Z. All authors have read and agreed to the published version of the manuscript.

Funding: This study was supported by the National Natural Science Foundation of China (Grant No. 41920104006) and the Scientific Research Fund of the Second Institute of Oceanography, Ministry of Natural Resources (Grant No. SZ2670).

Institutional Review Board Statement: Not applicable.

Informed Consent Statement: Not applicable.

Data Availability Statement: The wave observations supporting the findings of this study are available from the corresponding author upon reasonable request, subject to institutional data-sharing restrictions. ERA5 reanalysis data are publicly available from the Copernicus Climate Data Store (https://cds.climate.copernicus.eu/ (accessed on 16 July 2025)). MetOp-B and MetOp-C ASCAT Level-2 coastal wind data used for ERA5 wind validation were accessed through NASA's Earthdata Search portal (https://search.earthdata.nasa.gov/ (accessed on 20 October 2026)). (https://osi-saf.eumetsat.int/), (https://podaac.jpl.nasa.gov/). Tropical cyclone best-track data are available from the Shanghai Typhoon Institute of the China Meteorological Administration (CMA-STI). Bathymetric data were obtained from the ETOPO global relief dataset. The MATLAB (Version R2024a; MathWorks, Natick, MA, USA) scripts used for data processing and figure generation are available from the corresponding author upon reasonable request.

Acknowledgments: We thank the captain, crew, and research team involved in the field campaign for their assistance with wave observations and data collection.

Conflicts of Interest: The authors declare no conflicts of interest. The funders had no role in the design of the study; in the collection, analyses, or interpretation of data; in the writing of the manuscript; or in the decision to publish the results.

References

1. Wang, Z.; Li, S.; Dong, S.; Wu, K.; Yu, H.; Wang, L.; Li, W. Extreme wave climate variability in South China Sea. *Int. J. Appl. Earth Obs. Geoinf.* **2018**, *73*, 586–594. [CrossRef]
2. Jiang, S.H.; Shu, X.J.; Wang, Q.; Yan, Z.T. Evolution characteristics of wave energy resources in Guangdong coastal area based on long time series ERA-Interim reanalysis data. *Ocean Bull.* **2021**, *40*, 550–558.
3. Zhang, B.; Li, X.; Wang, L.; Gao, Y. Numerical simulation of typhoon waves in an offshore wind farm area of the South China Sea. *J. Mar. Sci. Eng.* **2025**, *13*, 451. [CrossRef]
4. Jia, L.Q.; Wu, S.M.; Han, B.; Cai, S.Q.; Wu, R.H. Wave hindcast under tropical cyclone conditions in the South China Sea: Sensitivity to wind fields. *Acta Oceanol. Sin.* **2023**, *42*, 36–53. [CrossRef]
5. Dong, S.; Gong, Y.; Wang, Z. Long-term variations of wind and wave conditions in the Taiwan Strait. *Reg. Stud. Mar. Sci.* **2020**, *36*, 101256. [CrossRef]
6. Hisaki, Y. Variability of wave height in the Sea of Japan. *Cont. Shelf Res.* **2022**, *233*, 104631. [CrossRef]
7. Dehghan, Y.; Sadrinasab, M.; Chegini, V. Probability distribution of wind speed and wave height in Nowshahr Port using the data acquired from wave scan buoy. *Ocean Eng.* **2022**, *252*, 111234. [CrossRef]
8. Xu, X.; Tao, A.; Li, X.; Zheng, X.; Lin, Y. Analysis of wave characteristics in the Central Taiwan Strait based on measured data. *J. Trop. Oceanogr.* **2021**, *40*, 12–20. Available online: https://www.jto.ac.cn/EN/Y2021/V40/I1/12 (accessed on 25 October 2026).
9. Yin, Y.; Jiang, L.; Zhang, Z.; Yu, H.; Wang, H. Statistical analysis of wave characteristics in the Pearl River Estuary. *J. Trop. Oceanogr.* **2017**, *36*, 60–66. Available online: https://www.jto.ac.cn/EN/10.11978/2016099 (accessed on 25 October 2026).
10. Chen, Y.Z.; Cao, Y.G.; Huang, Y.S.; Feng, Y.Q.; Liu, C.J.; Li, R.X.; Liao, S.Z.; Dong, C. Analysis on wave characteristics in Haikou Bay. *Ocean Eng.* **2019**, *37*, 96–103. [CrossRef]
11. Zhou, Y.; Ye, Q.; Shi, W.Y.; Yang, B.; Song, Z.K.; Yan, D.H. Wave characteristics in the nearshore waters of Sanmen Bay. *Appl. Ocean Res.* **2020**, *101*, 102236. [CrossRef]
12. Zhou, Y.; Li, Z.M.; Pan, Y.; Bai, X.L.; Wei, D.Z. Distribution characteristics of waves in Sanmen Bay based on field observation. *Ocean Eng.* **2021**, *229*, 108999. [CrossRef]
13. Chen, W.Y.; Liu, J.L.; Li, J.M.; Sun, L.; Li, B.; Xing, H.; Shi, P. Wave energy assessment for the nearshore region of the northern South China Sea based on in situ observations. *Energy Rep.* **2022**, *8*, 149–158. [CrossRef]
14. Cai, Z.W.; Chen, W.W.; Liu, X.L.; Sun, Z.; Ding, J. Characteristics of waves inside a lagoon of the South China Sea. *Ocean Eng.* **2020**, *208*, 107404. [CrossRef]
15. Yang, B.; Shi, W.Y.; Ye, Q.; Zhang, Z.L.; Yang, W.K.; Song, Z.K. Characteristics of waves in coastal waters of northeast Zhoushan Island during typhoons. *Adv. Water Sci.* **2017**, *28*, 106–115. [CrossRef]
16. Kumar, V.S.; Harikrishnan, S.; Mandal, S. Wave crest height distribution during the tropical cyclone period. *Ocean Eng.* **2020**, *197*, 106899. [CrossRef]
17. Yang, S.; Hou, Y.; Liu, Y. Observed typhoon wave spectrum in northern South China Sea. *Chin. J. Oceanol. Limnol.* **2015**, *33*, 1286–1294. [CrossRef]
18. Cai, Z.W.; Chen, W.W.; Liu, X.L.; Sun, Z. Observations of typhoon waves in a reef lagoon of the South China Sea. *J. Phys. Oceanogr.* **2020**, *50*, 161–173. [CrossRef]
19. Lai, S.K.; He, Y.; Chan, P.W.; Kerns, B.W.; Chen, S.S.; Su, H. Towards Skillful Tropical Cyclone Forecasting by AI-Model-Driven High-Resolution Regional Coupled Model. *Meteorol. Appl.* **2025**, *32*, e70109. [CrossRef]
20. Qiu, X.; Wei, W.; Chen, W.; Chen, Z.; Xie, D.; Cai, H. Storm-induced transformation in wave attenuation by mangroves: Couplings between surges and waves. *J. Hydrol.* **2026**, *664*, 134389. [CrossRef]
21. Lui, Y.S.; Cheung, P.; Tang, W.H.; Yeung, H.Y.; Lai, S.K.; Tse, W.P.; Lai, K.K.; Chan, P.W.; He, J.Y. An Observational and Forecast Study of Super Typhoon Fung-Wong in 2025 over the South China Sea. *Earth Space Sci.* **2026**, *13*, e2025EA004933. [CrossRef]
22. Liang, G.; Yang, J.; Wang, J. Accuracy Evaluation of CFOSAT SWIM L2 Products Based on NDBC Buoy and Jason-3 Altimeter Data. *Remote Sens.* **2021**, *13*, 887. [CrossRef]
23. Tang, S.; Chu, X.; Jia, Y.; Li, J.; Liu, Y.; Chen, Q.; Li, B.; Liu, J.; Chen, W. An Appraisal of CFOSAT Wave Spectrometer Products in the South China Sea. *Earth Space Sci.* **2022**, *9*, e2021EA002055. [CrossRef]
24. Xu, Y.; Hauser, D.; Liu, J.; Si, J.; Yan, C.; Chen, S.; Meng, J.; Fan, C.; Liu, M.; Chen, P. Statistical Comparison of Ocean Wave Directional Spectra Derived from SWIM/CFOSAT Satellite Observations and from Buoy Observations. *IEEE Trans. Geosci. Remote Sens.* **2022**, *60*, 5117520. [CrossRef]
25. Rybalko, A.; Myslenkov, S.; Badulin, S. Wave Buoy Measurements at Short Fetches in the Black Sea Nearshore: Mixed Sea and Energy Fluxes. *Water* **2023**, *15*, 1834. [CrossRef]
26. Ying, M.; Zhang, W.; Yu, H.; Lu, X.; Feng, J.; Fan, Y.; Zhu, Y.; Chen, D. An overview of the China Meteorological Administration tropical cyclone database. *J. Atmos. Ocean. Technol.* **2014**, *31*, 287–301. [CrossRef]
27. Lu, X.Q.; Yu, H.; Ying, M.; Zhao, B.K.; Zhang, S.; Lin, L.M.; Bai, L.N.; Wan, R.J. Western North Pacific tropical cyclone database created by the China Meteorological Administration. *Adv. Atmos. Sci.* **2021**, *38*, 690–699. [CrossRef]

28. Datawell BV. *Datawell Waverider Reference Manual: DWR-MkIII, DWR-G, WR-SG*; Datawell BV: Haarlem, The Netherlands, 2025.
29. Chu, X.; He, Y.; Chen, G. Asymmetry and anisotropy of microwave backscatter at low incidence angles. *IEEE Trans. Geosci. Remote Sens.* **2012**, *50*, 4014–4024. [CrossRef]
30. Chu, X.; He, Y.; Karaev, V.Y. Relationships between Ku-band radar backscatter and integrated wind and wave parameters at low incidence angles. *IEEE Trans. Geosci. Remote Sens.* **2012**, *50*, 4599–4609. [CrossRef]
31. Liu, T.M.; Yu, J.X.; Yu, Y.; Huang, H.; Zhang, X.W.; Zhou, B.C. Statistical characteristics of sea surface waves derived from buoy measurements in the eastern Guangdong offshore water. *J. Sea Res.* **2023**, *195*, 102440. [CrossRef]
32. Longuet-Higgins, M.S. On the statistical distribution of the heights of sea waves. *J. Mar. Res.* **1952**, *11*, 245–266.
33. Gao, C.C.; Zhou, G.C.; Wang, K.R. Study on wave characteristics in the nearshore waters of Xiangshui. *Acta Oceanol. Sin.* **2019**, *41*, 23–34.
34. Yang, Z.; He, H.; Gao, Z. Statistical distribution and spectral analysis of wave of Chiwan Bay. *Water Transp. Eng.* **1986**, *12*, 5–10.
35. Goda, Y.; Nagai, Y. Investigation and analysis of statistical characteristics of waves. *Rep. Port Harb. Res. Inst.* **1974**, *13*, 3–37.
36. Yu, Y.X.; Liu, S.X. Statistical characteristics and wave spectrum of sea waves in Shijiu Port. *Port Eng. Technol.* **1989**, *2*, 12–22.
37. Ge, M.D. Distributions of wave heights and periods in Lianyun Harbour. *Ocean Eng.* **1984**, *1*, 40–50.

Disclaimer/Publisher's Note: The statements, opinions and data contained in all publications are solely those of the individual author(s) and contributor(s) and not of MDPI and/or the editor(s). MDPI and/or the editor(s) disclaim responsibility for any injury to people or property resulting from any ideas, methods, instructions or products referred to in the content.